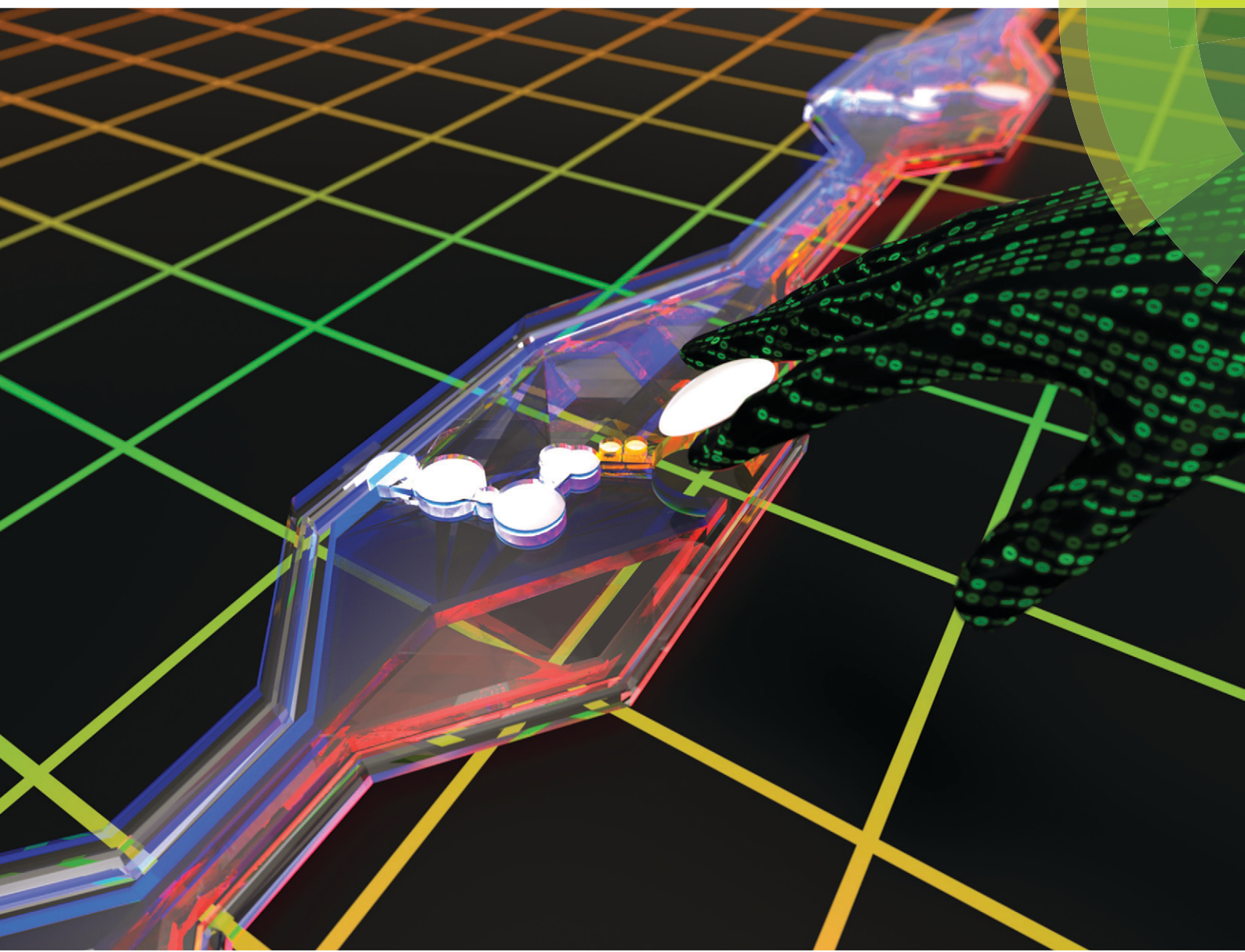


# Lab on a Chip

Devices and applications at the micro- and nanoscale

rsc.li/loc



ISSN 1473-0197



ROYAL SOCIETY  
OF CHEMISTRY

Celebrating  
IYPT 2019

PAPER

J. Wang, N. Zhang *et al.*

Finding the optimal design of a passive microfluidic mixer

Cite this: *Lab Chip*, 2019, **19**, 3618

## Finding the optimal design of a passive microfluidic mixer†

Junchao Wang, <sup>a,b</sup> Naiyin Zhang, <sup>a,c</sup> Jin Chen,<sup>a</sup> Victor G. J. Rodgers,<sup>b</sup> Philip Brisk<sup>d</sup> and William H. Grover <sup>\*b</sup>

The ability to thoroughly mix two fluids is a fundamental need in microfluidics. While a variety of different microfluidic mixers have been designed by researchers, it remains unknown which (if any) of these mixers are optimal (that is, which designs provide the most thorough mixing with the smallest possible fluidic resistance across the mixer). In this work, we automatically designed and rationally optimized a microfluidic mixer. We accomplished this by first generating a library of thousands of different randomly designed mixers, then using the non-dominated sorting genetic algorithm II (NSGA-II) to optimize the random chips in order to achieve Pareto efficiency. Pareto efficiency is a state of allocation of resources (e.g. driving force) from which it is impossible to reallocate so as to make any one individual criterion better off (e.g. pressure drop) without making at least one individual criterion (e.g. mixing performance) worse off. After 200 generations of evolution, Pareto efficiency was achieved and the Pareto-optimal front was found. We examined designs at the Pareto-optimal front and found several design criteria that enhance the mixing performance of a mixer while minimizing its fluidic resistance; these observations provide new criteria on how to design optimal microfluidic mixers. Additionally, we compared the designs from NSGA-II with some popular microfluidic mixer designs from the literature and found that designs from NSGA-II have lower fluidic resistance with similar mixing performance. As a proof of concept, we fabricated three mixer designs from 200 generations of evolution and one conventional popular mixer design and tested the performance of these four mixers. Using this approach, an optimal design of a passive microfluidic mixer is found and the criteria of designing a passive microfluidic mixer are established.

Received 9th June 2019,  
Accepted 16th September 2019

DOI: 10.1039/c9lc00546c

rsc.li/loc

## 1 Introduction

Mixing is one of the fundamental functions in microfluidic chips. For the past decade, a wide variety of different microfluidic mixers have been designed.<sup>1</sup> Microfluidic mixers are usually categorized as either “active” (an external energy force or an external physical field is present to accelerate mixing phenomenon) or “passive” (mixing is accomplished only by diffusion and is dependent only on the area of contact between the two fluids and the amount of time the fluids are

in contact). Active mixers generally outperform passive mixers, but integrating an external force or field in the chip adds unwanted complexity and cost. Passive mixers are simpler and more economical, but increasing the area and time of contact between the two fluids has undesirable consequences: increasing contact area by lengthening the channel containing the two fluids adds unwanted additional fluidic resistance to the channel, and increasing contact time by slowing the flow rate decreases the overall throughput of the microfluidic chip.<sup>2</sup> Thus, there is an unmet need for mixer designs that combine high mixing performance with low fluidic resistance and high flow rates.

Several studies have been conducted on the optimization of standard microfluidic mixer designs. Li *et al.* optimized a chaotic microfluidic mixer using lattice Boltzmann method.<sup>3</sup> Hertzog *et al.* used an optimized microfluidic mixer to study the protein folding kinetics.<sup>4</sup> Two continuous studies from Wang *et al.* focused on the optimization of the layout of obstacles for enhanced mixing in microchannels for different applications using a fluid dynamics software.<sup>5,6</sup> Hossain *et al.* conducted research of optimizing a modified Tesla structure based on topology optimization.<sup>7</sup> Finally, Cortes-

<sup>a</sup> Key Laboratory of RF Circuits and Systems, Ministry of Education, and Zhejiang Provincial Laboratory of Integrated Circuit Design, Hangzhou Dianzi University, China. E-mail: junchao@hdu.edu.cn; Tel: +86 571 8691 9078

<sup>b</sup> Department of Bioengineering, University of California Riverside, Riverside, CA, USA. E-mail: wgrover@engr.ucr.edu; Tel: +1 951 827 4311

<sup>c</sup> College of Life Information Science and Instrument Engineering, Hangzhou Dianzi University, China

<sup>d</sup> Department of Computer Science and Engineering, University of California Riverside, Riverside, CA, USA

† Electronic supplementary information (ESI) available. See DOI: 10.1039/c9lc00546c

‡ These authors contributed equally to this work.

Quiroz *et al.* optimized a grooved microfluidic mixer using a multi-objective optimization approach.<sup>8</sup> In these optimization processes, the design criteria of the post-optimized mixer designs remained unchanged compared to their original designs, which results in a limited improvement of the mixing performance. For instance, Hossain *et al.* optimized the mixing performance of the Tesla structure mixer, but the basic design of the mixer remained unchanged.<sup>7</sup>

Occasionally, researchers develop new microfluidic mixer designs that have advantages over existing designs. For example, Fu *et al.* designed a rapid vortex microfluidic mixer utilizing double-heart chambers that achieved a 92% mixing ratio at Reynolds numbers as low as  $Re = 1$  (ref. 9) and Wang *et al.* used triangular posts in a conventional Y-shaped microfluidic mixer to increase the mixing performance.<sup>10</sup> But are these mixer designs really optimal, or are there better designs waiting to be discovered? With an infinite variety of possible designs, and only a relatively small number of researchers exploring this design space, progress toward better mixers is frustratingly slow.

This situation inspired us to ask, is it possible to design a microfluidic mixer from scratch by computer algorithm without needing microfluidics expertise at design phase? If so, is it possible that these automatically-designed mixers will

give us new useful design criteria to use when manually designing mixers?

In this work, we set out to answer the question, is it possible to find the most optimized mixer within certain conditions? Specifically, are we able to explore the performance boundary of how good a microfluidic mixer can possibly be within a certain limit on fluidic resistance?

Here, we developed an approach to automatically design and optimize passive microfluidic mixers for specific conditions. We accomplished this in two steps. First, we generated a library of more than six thousand different random mixer designs and simulated the performance of each of them. We have previously used this technique to generate designs of functional microfluidic chips that can deliver solutes of any desired concentrations.<sup>11</sup> Second, we used the non-dominated sorting genetic algorithm II (NSGA-II)<sup>12</sup> to optimize multiple design parameters of our microfluidic mixer at the same time. NSGA-II is one of the multi-objective evolutionary algorithms (MOEAs), which helped our mixer designs to increase their mixing performance, achieve Pareto efficiency, and find the Pareto-optimal front. Pareto efficiency is a state of allocation of resources (e.g. fluid driving force) from which it is impossible to reallocate so as to make any one individual

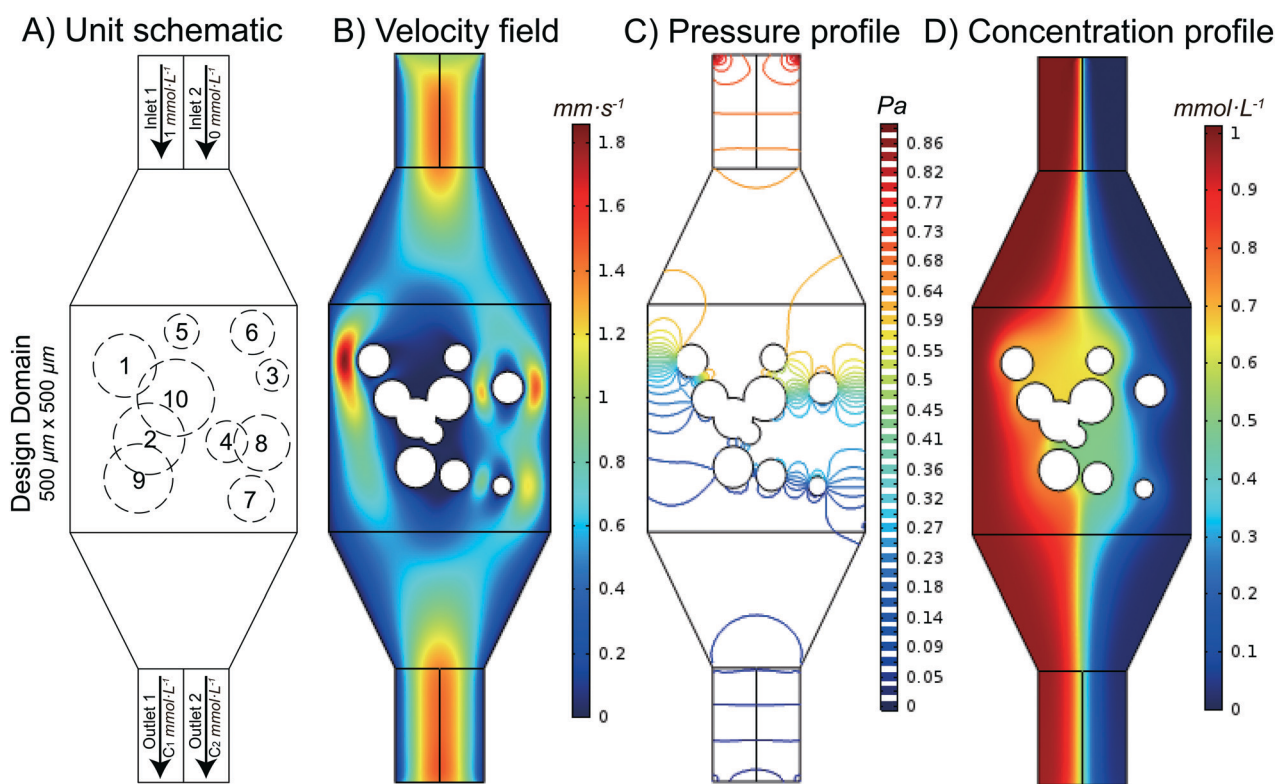


**Fig. 1** (A) Schematic of a simulated microfluidic mixer unit. A simulated unit has two inlets and two outlets. Between inlets and outlets is a 500  $\mu\text{m} \times 500 \mu\text{m}$  design domain. In the design domain, each mixer has ten cylindrical posts with random sizes and locations. Different cylinder posts were allowed to overlap to create additional structures like walls. (B) The predicted fluid velocity field of a typical mixer unit. This velocity field is used for simulating the solute concentration profile in the mixer. (C) The predicted pressure profile of the mixer unit. This pressure profile is used to characterize the fluidic resistance of the mixer. (D) The predicted solute concentration profile of the mixer unit. This concentration profile is used to determine the mixing performance of this mixer unit.

criterion better off (*e.g.* pressure drop) without making one or more individual criterion (*e.g.* mixing performance) worse off. The Pareto-optimal front is the set of all Pareto efficient allocations, which is conventionally visualized as a boundary in a graph of performance. To investigate the Pareto efficiency of our system, random mixer designs and NSGA-II mixer designs were visualized in the same graph (Fig. 4A) of mixing performance *vs.* fluidic resistance.

Our results showed that after 200 generations of evolution, the mixer designs converged near the true Pareto-optimal front; this allowed us to explore the fundamental performance limits of a microfluidic mixer. A user can select a design from these optimized mixers and be confident that the design is optimal for a given fluidic resistance. Additionally, we identified certain design trends in the optimized mixers, manually designed several mixers that incorporate these trends, and compared the performance of our manually-designed mixers to that of our automatically-designed optimal mixers. In each case, our automatically-designed and optimized mixers equaled or exceeded the mixing performance of conventional designed mixers. Finally, to confirm that the mixers designed by our algorithm function as predicted, we chose three optimum mixer designs at corresponding minimized resistance conditions from the Pareto-optimal front and one chip from conventional designed mixers and fabricated corresponding polydimethylsiloxane (PDMS) microfluidic chips for experimental verification.

## 2 Materials and methods

### 2.1 Generating initial random mixer designs

We created our first generation of passive microfluidic mixers by generating mixer designs at random.<sup>11</sup> Of course, there is an essentially limitless variety of possible mixer designs, so we applied certain constraints to our random designs. Fig. 1A shows the basic design template of our random mixers. Each mixer has two inlets, two outlets, and a 500  $\mu\text{m} \times 500 \mu\text{m}$  design domain where the random mixing structures are located. In the design domain are ten cylindrical posts with random sizes and locations. Ten cylindrical structures were chosen as a balance between computational resources and achieving as many different mixing features as possible within a 500  $\mu\text{m} \times 500 \mu\text{m}$  design domain. Each cylindrical structure acted as a building unit of the mixing features in each design, and ten cylindrical structures were good enough to represent the diversity of mixing features. For example, two or more cylindrical posts can overlap, which enables the mixer designs to also include non-circular features (*like* walls, inverted-L or S-shape). In addition, cylindrical structures naturally create smoother fluid streamlines than square or triangular structures, which is helpful for reducing the overall fluidic resistance of the mixer. In total, 6096 different mixer designs were generated and stored in a database. Finally, in addition to randomly-generated designs, we also manually designed five mixer units based on our experience so as to compare them with the randomly

generated designs as well as NSGA-II designs. The specific code we write to generate 6069 mixer designs is available in ESI.<sup>†</sup>

### 2.2 Simulating mixer performance

All simulations were performed using the finite element analysis software COMSOL Multiphysics (COMSOL Inc., Burlington, MA). We used the software's MATLAB API to automate the simulation process. The laminar flow physics module and transport of dilute species physics module as well as two stationary solvers were used in COMSOL Multiphysics. In the laminar flow physics module in COMSOL Multiphysics, each inlet was assigned an inlet boundary condition of 1  $\text{mm s}^{-1}$  normal inflow velocity, and each outlet was assigned an outlet boundary condition of 0 Pa pressure. The remaining boundaries were walls (no-slip boundary condition), and the material filling the channels was water under incompressible flow. In the transport of dilute species physics module, inlet 1 is assigned an inflow concentration of 1  $\text{mmol L}^{-1}$  and inlet 2 is assigned an inflow concentration of 0  $\text{mmol L}^{-1}$ . The two outlets were assigned as outflows. The solute diffusion coefficient of fluorescein ( $4.25 \times 10^{-10} \text{ m}^2 \text{ s}^{-1}$ ) was used in simulation in order to represent the mixing behavior of small molecules.<sup>13</sup> Fig. 1B and C show the calculated velocity field and pressure field of one mixer unit design, and Fig. 1D shows the concentration mixing field of the same design. The corresponding script for simulating the performance of the mixer designs is available in ESI.<sup>†</sup>

### 2.3 Evolving mixer designs with NSGA-II

The genetic algorithm NSGA-II<sup>12</sup> was used to evolve optimized versions of our passive random mixers. A flow chart representation of our custom NSGA-II implementation is shown in Fig. 2. The fitness function for fluidic resistance ( $S_P$ ) is

$$S_P = P_2 - P_1 \quad (1)$$

where  $P_2$  is the pressure at the outlets and  $P_1$  is the pressure at the inlets. This means that the smaller the pressure drop across the mixer, the better the performance of the mixture. The fitness function for mixing performance is defined as the mixing score ( $S_C$ ),

$$S_C = (1 - C_1) + (C_2 - 0) \quad (2)$$

where  $C_1$  is the average concentration of outlet 1;  $1 - C_1$  calculates the average concentration difference between inlet 1 and outlet 1;  $C_2$  is the average concentration of outlet 2;  $C_2 - 0$  calculates the average concentration difference between inlet 2 and outlet 2. This indicates that the closer the concentrations of the fluids in outlet 1 and outlet 2, the better performance of the mixer. Eqn (2) is not our only choice for quantifying the mixing performance. For example,

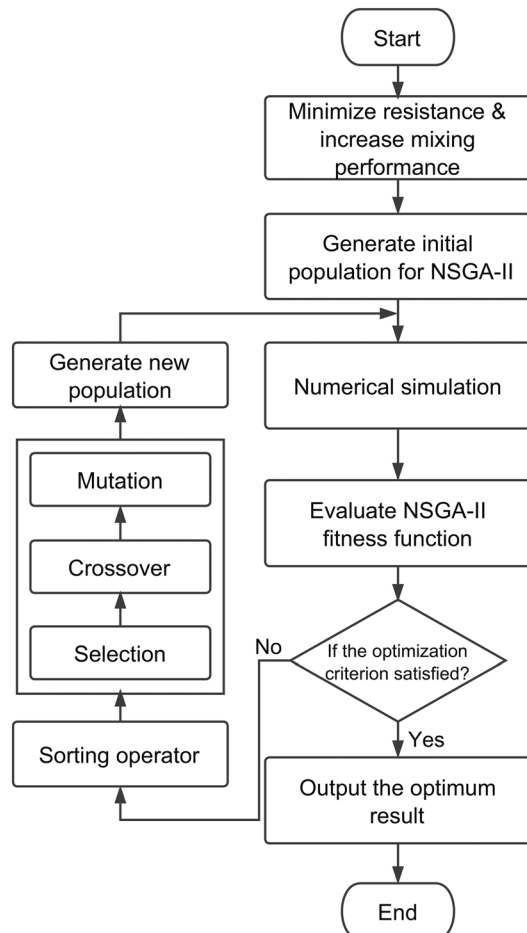


**Fig. 2** A flow chart depicting our custom NSGA-II process for optimizing mixers and finding the Pareto-optimal front. The overall goal was to minimize the pressure drop (fluidic resistance) of mixer designs while increasing the mixing performance. Numerical simulation was conducted by COMSOL Multiphysics and MATLAB. Typical genetic operators (selection, crossover, mutation) were conducted after a non-dominant sorting operator. After that, the population of next generation mixer designs were generated and repeated in the loop until the optimization criterion was satisfied.

$((1 - C_1) + (C_2 - 0))^2$  or  $C_1/C_2$  are acceptable fitness functions as well. However, eqn (2) has several advantages in this study. For example, eqn (2) results in a range of scores that is normalized from 0 to 1. For instance, a perfectly mixed solution would have  $C_1 = C_2 = 0.5 \text{ mmol L}^{-1}$ ,  $S_C$  would equal 1; a perfectly un-mixed solution would have  $C_1 = 1 \text{ mmol L}^{-1}$ ,  $C_2 = 0 \text{ mmol L}^{-1}$ ,  $S_C$  would equal 0. Additionally, since eqn (1) had been defined as a first-order equation, it was natural to define the fitness function for mixing performance as a first-order equation as well because both optimization criteria are equally important in our optimization process. Using fitness function like  $((1 - C_1) + (C_2 - 0))^2$  for mixing performance would probably yield similar results. However, plots of the Pareto-optimal front would be distorted by the non-uniform spacing of mixing scores. For these reasons, eqn (2) was used to quantify the mixing performance in this work.

Out of all 6069 random mixer designs, one design was chosen as generation 0 ( $G_0$ , the parent of first generation in our evolutionary algorithm).  $G_0$  was chosen for two reasons. First,  $G_0$  is one of the top performers, which is located at the edge of all random designs in the pressure drop vs. mixing score map (Fig. 4A), a location that might already be close to the Pareto-optimal front. Second, after investigating the post layout of  $G_0$ , we found all ten cylindrical posts were located around the center region of the design domain, which might let our algorithm to have a higher probability to explore as many post layouts as possible in a limited number of evolution runs. The non-dominant sorting operation, selection, crossover, and mutation operators were then conducted so as to generate the new population of designs. After that, numerical simulations were performed using the same simulation parameters as the randomly generated designs above. In total, 200 generations were calculated to find the Pareto-optimal front. The corresponding guidelines for implementing NSGA-II for specific applications are available in ESI.<sup>†</sup>

#### 2.4 The robustness of NSGA-II

NSGA-II is one of the most popular multi-objective evolutionary algorithms (MOEAs), and the algorithm has been applied in many different fields.<sup>14–17</sup> To verify the performance and robustness of MOEAs, computer scientists have developed guidelines and carefully selected a number of test problems.<sup>18,19</sup> The objective functions of these test problems are complicated mathematical functions, whose graphs could be convex, nonconvex, disconnected or even nonuniformly spaced. Computer scientists then used MOEAs to find the minimum solutions which were satisfying all the objective functions at the same time. After testing with nine test problem sets, NSGA-II demonstrated strong robustness among different MOEAs.<sup>12</sup>

#### 2.5 Functional chip design, fabrication and experiments

Design generation 0 ( $G_0$ ), generation 60 ( $G_{60}$ ), generation 120 ( $G_{120}$ ) and conventional design C (shown in Fig. 4) were chosen to be fabricated by conventional soft-lithography.<sup>20</sup> Since each mixer unit (Fig. 1) predicted by our method has limited mixing performance in the  $500 \mu\text{m} \times 500 \mu\text{m}$  design domain, we put 11 identical mixing units in a chain to amplify the mixing performance. As shown in Fig. 3A and C, each fabricated microfluidic mixer has 11 mixing units and each mixing unit duplicates the structure of the design domain from  $G_0$ ,  $G_{60}$ ,  $G_{120}$ , and conventional design C. Treating all 11 copies of each mixer identically is not ideal. However, our decision to do so represents a trade-off between two practical issues. On one hand, since the amount of mixing provided by a single mixer is rather small and would be difficult to accurately quantify experimentally, we needed a way to amplify the net mixing we observed in our experiments. On the other hand, we recognize that the second mixer in a series receives a slightly different concentration profile than the first mixer, the third mixer receives a different

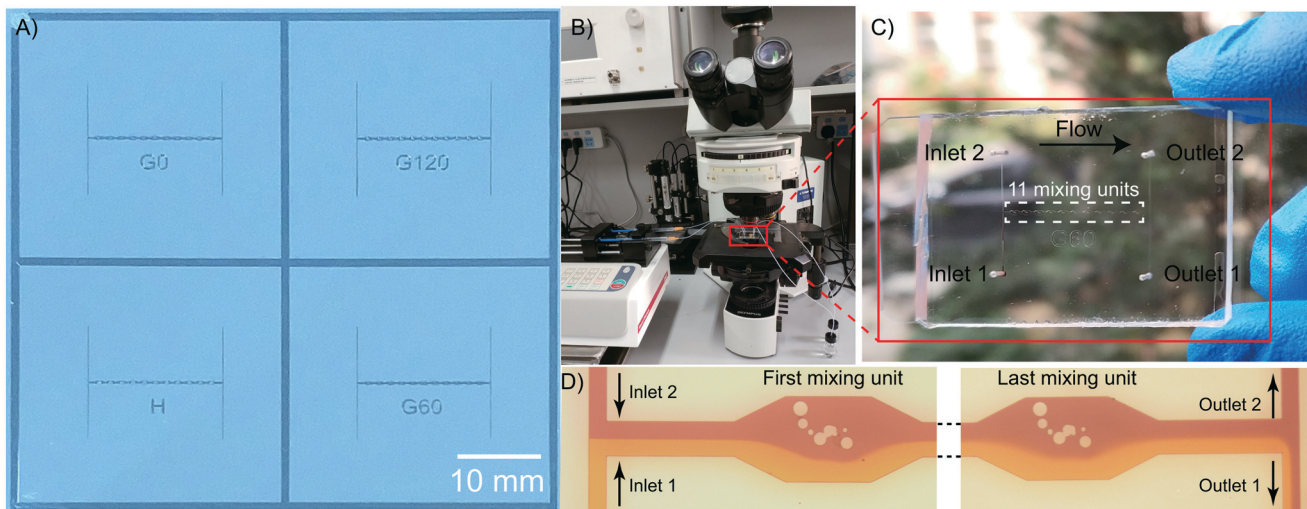


**Fig. 3** (A) The SU-8 mold of mixer designs G0, G60, G120, and conventional design C. (B) In each case inlet 1 was injected with FD&C Blue #1 and inlet 2 was injected with FD&C Red #3. Silastic laboratory tubings were used to connect the syringe pump and sample reservoirs with the microfluidic mixers. Post-mixed fluids were collected in these reservoirs for quantification of the mixing performance. (C) Photographs of the G60 microfluidic mixer. As with all designs, this G60 microfluidic mixer has two inlets and two outlets. The main channel consists of 11 identical mixing units, each of which corresponds to the structure of pre-simulated G60 design. (D) Photographs of the first mixing unit and the last mixing unit of G60 microfluidic mixer in operation. Two dyes (red color from the top inlet, and orange color from the bottom inlet) flow into the chip. The different layouts created by the 10 posts in the design domain affected the mixing performance and the resistance of each mixer design, causing the two fluids to be significantly mixed after passing through 11 mixing units and exiting through the two outlets.

profile than the second, and so on. Accurately predicting the unique behavior of the N unit mixer would require knowledge of the unique behavior of all N-1 unit mixers upstream. This interdependence would add enormous computational complexity to our task: finding an optimal series of different mixer designs would require simulating and optimizing thousands of versions of all 11 designs connected together, a computational task that is far outside of our capabilities. As a trade-off between experimental verification and computational feasibility, we experimentally tested different mixer designs using 11 identical copies of each mixer.

The main features (cylindrical posts) of the mixer were designed by our algorithms and exported into DXF files.<sup>21</sup> Based on these DXF files, additional features including inlets and outlets were designed manually in AutoCAD (Autodesk, San Rafael, CA) and then written to a transparent mask. Negative photoresist (SU-8 25, Microchem, MA) was spin-coated on a 4 inch polished silicon wafer to fabricate the SU-8 mold as shown in Fig. 3A. The channel width was 200  $\mu\text{m}$  and the channels depth was 50  $\mu\text{m}$ , which was consistent with our simulation models. After that, a volumetric ratio of 10:1 mixture of PDMS (Sylgard 184, Dow Corning, MI) and curing agent were poured onto the SU-8 mold. After degassing and curing, the PDMS replica was peeled off from the master and punched on top for inlet and outlet. Finally, a plasma cleaner was used to change the surface properties of the PDMS replica and the glass slides in order to create a PDMS-glass bond.

As shown in Fig. 3B, a dual channel syringe pump was used to provide the driving force for the microfluidic mixers (although we expect that pressure-driven flow using identical

pressures at each inlet will give similar results, since the two sets of inlet and outlet channels in our mixer chips have the same length and resistance to flow). The volumetric flow rate for each syringe was set to 3  $\mu\text{L min}^{-1}$ . The inlets of chips were connected to the syringes by Silastic laboratory tubing (Dow Corning, Michigan, US) and the outlets were connected to the sample reservoirs by tubing as well. Fig. 3D shows the first mixing unit and the last mixing unit of G60 microfluidic mixer in operation. For visualization, inlet 1 contains a dye that appears orange on our imaging system (FD&C Red #3) and inlet 2 contains a dye that appears red (FD&C Blue #1). The chips were imaged using an optical microscope (Olympus BX51, Tokyo, Japan). For quantification of the mixing performance, inlet 1 was injected with water and inlet 2 was injected with FD&C Red #3. To make sure that the system reached steady state and all the air bubbles went away, samples were collected from the chip after 5 minutes of flow and visual confirmation for the nonexistence of bubbles in the channels was conducted with the microscope. After that, samples from both outlets were collected into tubes. A standard curve was plotted based on standard dye concentration. Both the standard curve and samples were analyzed using a UV-VIS-NIR spectrophotometer at 530 nm (Shimadzu UV3600, Kyoto, Japan). Finally, the concentration of each sample was calculated using the standard curve.

## 3 Results and discussion

### 3.1 Finding the Pareto-optimal front

Fig. 4A plots pressure drop *versus* mixing score for each of the randomly-generated designs (small blue circles), NSGA-

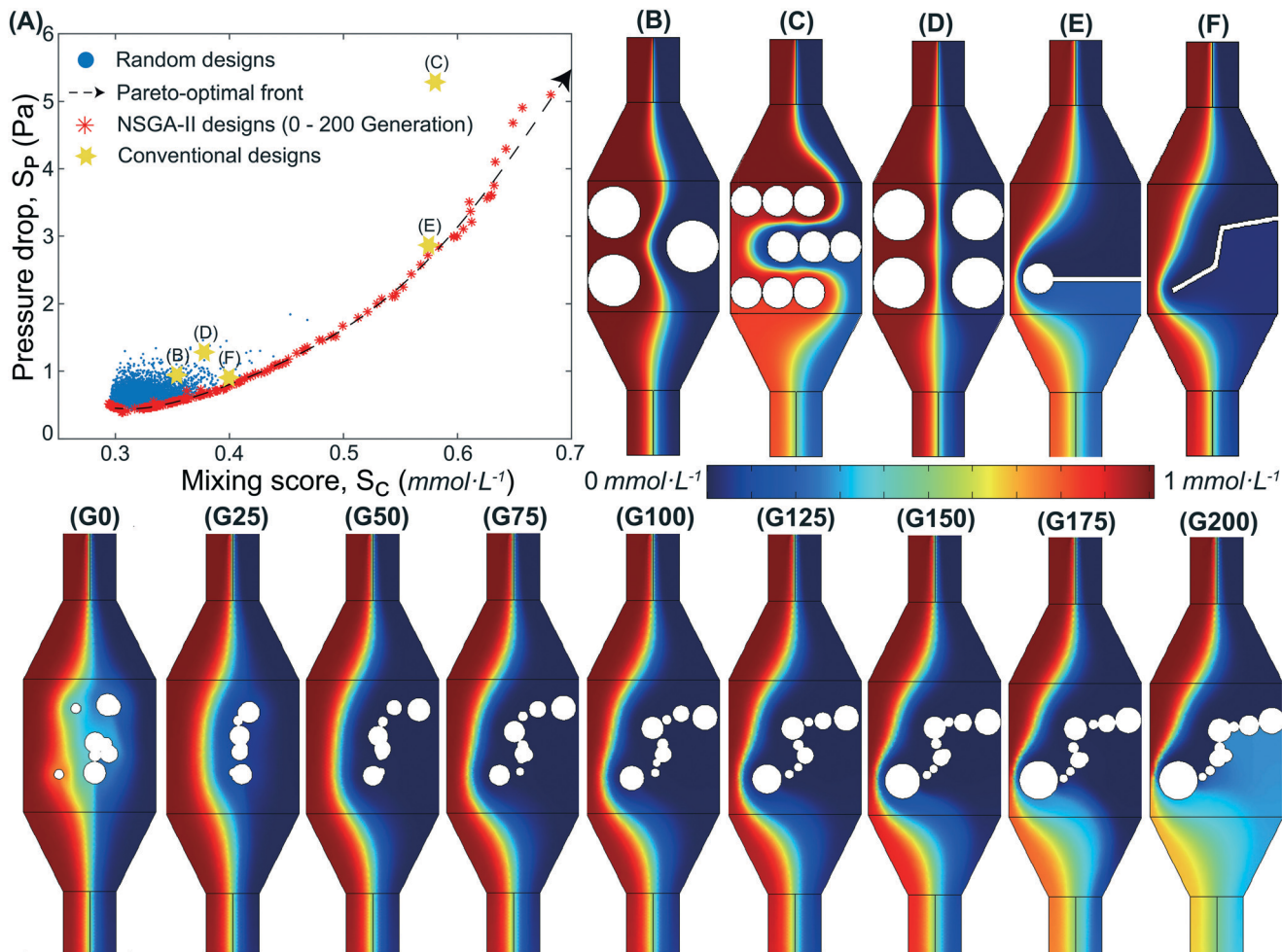


**Fig. 4** (A) Pressure drop ( $S_P$ ) vs. mixing score ( $S_C$ ) for random microfluidic mixer designs (blue dots) and NSGA-II-evolved mixer designs (red stars). The random designs are distributed in the bottom-left corner while the NSGA-II designs are at the boundary of all random designs. By connecting all the NSGA-II designs, we can draw a Pareto-optimal front (dashed line). Conventional designs (B–F) (yellow stars) lie above the Pareto-optimal front, which means that their mixing performance is not as good as NSGA-II designs with a certain pressure drop. (G0–G200) The concentration profiles of NSGA-II designs of generation 0, 25, 50, 75, 100, 125, 150, 175 and 200. Additional concentration profiles, pressure profiles, and velocity fields of 0–200 generations are available in ESI.<sup>†</sup>

II-evolved optimal designs (red stars), and conventional designs (yellow stars). The NSGA-II designs distribute at the boundary of the randomly generated designs. This means that NSGA-II successfully found the Pareto-optimal front. To achieve a similar mixing score, NSGA-II designs always need less pressure drop or generate less resistance in a mixer unit. In other words, within a certain pressure drop condition, the NSGA-II designs will always have better mixing performance than the random-design mixers. Since G0 was randomly designed, its pressure drop still had space to be minimized. That is why we observed a small decrease in pressure drop during the initial 20 generations. After that, as the mixing score increased, the pressure drop increased as well.

Fig. 4B–D are three common microfluidic mixer designs being constrained to our design domain using cylinder posts to map the geometry. Conventional design B has a pressure drop of 0.98 Pa and a mixing score of 0.35  $\text{mmol}\cdot\text{L}^{-1}$ .

Conventional design C has a pressure drop of 5.36 Pa and a mixing score of 0.59  $\text{mmol}\cdot\text{L}^{-1}$ . Conventional design D has a pressure drop of 1.29 Pa and a mixing score of 0.38  $\text{mmol}\cdot\text{L}^{-1}$ . Adding their mixing performance to the plot in Fig. 4A (yellow stars) shows that designs B, C, and D all lie above the evolved designs (red stars). This tells us that the common mixer designs for microfluidics still have potential to be optimized.

Fig. 4 (G0–G200) are the concentration profiles of NSGA-II designs in generations 0, 25, 50, 75, 100, 125, 150, 175 and 200. As the generation number increases, the mixing performance improves and the mixer geometry converges into an S-shaped line of cylinders. The S-shape suggests that NSGA-II selects S-shaped designs as elite designs and retains the S-shaped feature into the next generations. The S-shape could increase the mixing contact area as well as minimizing the fluidic resistance. The small gaps between each post also appear to be crucial to the performance of the mixer. From

the concentration and pressure profiles of each generation (see ESI†), we know that each small gap allows fluid with no chance to mix (solute concentration around  $0 \text{ mmol L}^{-1}$ ) to go through the S-shape and reduce the overall fluidic resistance of the mixer. We are unaware of any similar designs that have been created by conventional manual design methods. Finally, Fig. 4E and F are manually-designed mixers that are inspired by NSGA-II designs. Conventional design E has a pressure drop of  $2.87 \text{ Pa}$  and a mixing score is  $0.59 \text{ mmol L}^{-1}$ . Conventional design F has a pressure drop of  $0.81 \text{ Pa}$  and a score of  $0.40 \text{ mmol L}^{-1}$ . Their performance (gold stars marked E and F on Fig. 4A) is close to the Pareto-optimal front but they do not have small gaps in dark blue area (solute concentration around  $0 \text{ mmol L}^{-1}$ ) to reduce the fluidic resistance.

### 3.2 Experimental verification

To demonstrate the functionalities of the automatically-designed microfluidic mixers, three evolved designs (G0, G60, and G120 in Fig. 4) and one of the conventional designs (C in Fig. 4) were chosen to be fabricated and tested. The concentration profiles of each last (11th) mixing unit of G0, G60, G120, and conventional design C in operation are shown in Fig. 5A. As generation number increased, the red fluid occupied more region in the design domain, invading the area of the orange fluid, which enhanced the mixing phenomenon. The small gaps created by posts in the red fluid region contributed to minimizing the fluidic resistance. The mixing in conventional design C simply relied on diffusion between two fluid without any structure to minimize the fluidic resistance. As shown in Fig. 5B, the mixing scores of G0, G60, G120 and conventional design C were  $0.459 \text{ mmol L}^{-1}$ ,  $0.498 \text{ mmol L}^{-1}$ ,  $0.613 \text{ mmol L}^{-1}$  and  $0.762 \text{ mmol L}^{-1}$ , respectively; and the predicted pressure drop of the 11 mixing units by COMSOL Multiphysics were  $5.5 \text{ Pa}$ ,  $5.39 \text{ Pa}$ ,  $8.36 \text{ Pa}$  and  $58.96 \text{ Pa}$ , respectively. After evolving for 120 generations, the mixing score improved by 33.6% while the cost (the pressure drop generated by 11 mixing units) increased by 52%. In contrast, though conventional design C had a better mixing score than G120 ( $0.762 \text{ mmol L}^{-1}$  vs.  $0.613 \text{ mmol L}^{-1}$ ), the pressure drop cost was tremendous ( $58.96 \text{ Pa}$  vs.  $8.36 \text{ Pa}$ ).

In order to mathematically quantify the performance of the mixers using the mixing score and the pressure drop, eqn (3) is defined as follows,

$$M_{\text{cost}} = \frac{S_p}{S_c} \quad (3)$$

where  $S_p$  is the pressure drop that is defined in eqn (1) and calculated by COMSOL Multiphysics;  $S_c$  is the mixing score defined in eqn (2) and measured by experiments;  $M_{\text{cost}}$  indicates the mixing cost of the mixers by calculating the fraction of the pressure drop and the mixing score. The physical meaning of  $M_{\text{cost}}$  is how much pressure (the driving force) we need in order to achieve  $1.0 \text{ mmol L}^{-1}$  mixing score. The  $M_{\text{cost}}$  of four tested mixers is summarized in Table 1. It

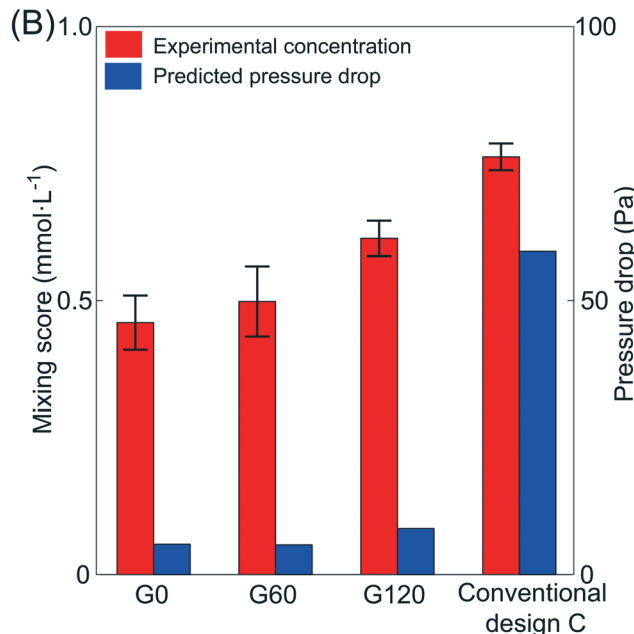
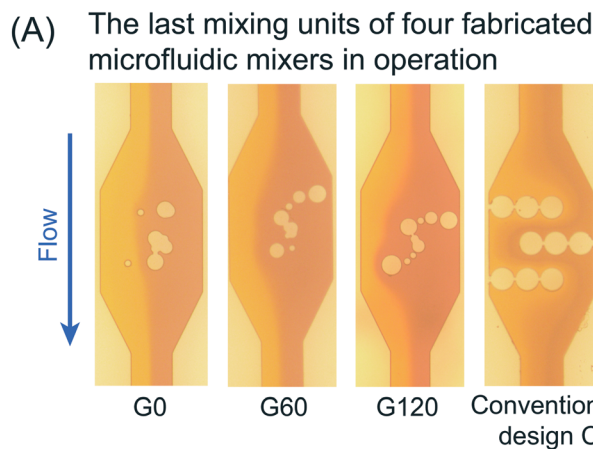


**Fig. 5** (A) The concentration profiles of each last (11th) mixing unit of G0, G60, G120, and conventional design C in operation. (B) Mixing scores and predicted pressure drop of four fabricated mixers. The left y-axis indicates the mixing score and the right y-axis indicates the predicted pressure drop of total 11 mixing units of each mixer. Three measurements were conducted for each point of the mixing scores; error bars indicate  $\pm 1$  standard deviation.

is clear that although conventional design C has a higher mixing score than G0, G60 or G120, its  $M_{\text{cost}}$  is more than 5 times higher than the  $M_{\text{cost}}$  of G0, G60 and G120 in average. The  $M_{\text{cost}}$  first dropped 10% from G0 to G60 and increased 25% from G60 to G120. Since G0 was randomly designed and only located close to the Pareto-optimal front, the 10% drop indicated that G0 to G60 was approaching the ideal Pareto-optimal front, in which the increase of  $S_c$  was along with the decrease of  $S_p$  in a certain range. The 25% increase indicated

**Table 1** Mixing cost of four tested mixers

	G0	G60	G120	Conventional design C
$M_{\text{cost}}$ (Pa mmol $^{-1}$ L)	12.0	10.9	13.7	76.9

that the mixer designs of G60 to G120 had lain on the Pareto-optimal front, in which the increase of  $S_C$  had to be along with the increase of  $S_P$  as well and the increment of  $S_P$  is larger than the increment of  $S_C$ . Overall, the  $M_{\text{cost}}$  gives us a quantitative way to calculate how much a specific mixer design can be optimized.

### 3.3 Rational design inspired by two separate evolution runs

Since we only have 200 populations in each generation while the size and position of cylinder posts in the design domain are infinite, the Pareto-optimal front we found is close to the ideal Pareto-optimal front theoretically. It is interesting to investigate how separate evolution runs will affect the design of mixers. Fig. 6 shows the comparison of NSGA-II designs between two separate evolution runs. Fig. 6A is the first run (the results are the same as those in Fig. 4). Fig. 6B is the second run, and in this run we found that the geometry converged into a Y-shape instead of an S-shape. While the mixing scores of these two separate evolution runs are similar

(around 0.68 mmol L<sup>-1</sup>), the design from the first run has a lower pressure drop. This indicates that the Pareto-optimal front found from the first run is closer to the ideal Pareto-optimal front. Although the geometries resulting from the two evolution runs are different, they do share two important similarities. First, they both created a narrow gap near the left edge with a large cylindrical post. Second, they used the rest of the cylinder posts to generate a wall containing small gaps in the dark blue area (around 0 mmol L<sup>-1</sup>) so as to minimize the pressure drop. So, why did the design from the first evolution run have a lower pressure drop? From the concentration profiles, we can see that in the first run design, fluid had a longer contact time and contact area before entering the critical gap (generated by the largest post). Additionally, it seems that the second-evolution designs only used eight posts to create a wall instead of ten. Two upper cylinder posts (pointed by gray arrows) seem to have no function but increase the fluidic resistance of this design.

The main reason two separate runs falls into two different local minimums is due to the limited populations in each generation. In order to get highly identical results between separated runs, we could include more populations in each generation. However, predicting the velocity fields and concentration profiles of more populations would be computationally expensive. It took us several hours to simulate 200 different velocity fields and concentration profiles for only one generation even the simulations were processed in a workstation with a Intel 10-core Xeon Silver CPU and 64 GB RAM. Fortunately, the comparison between two separated runs gave us a perfect example – if we want to reduce the overall pressure drop, we could design some gaps in the region where fluid get no chance to mix without hurting the overall mixing performance.

## 4 Conclusions

We demonstrated how to optimize a functional microfluidic mixer for two parameters, pressure drop and mixing score, using NSGA-II. We accomplished this by using MATLAB and COMSOL Multiphysics as our simulation platform and implementing NSGA-II in MATLAB. We found the pressure drop *versus* mixing score Pareto-optimal front. After that, we compared the designs at the Pareto-optimal front with conventional designs and random designs. Our simulations indicate that designs from NSGA-II have lower pressure drops than designs by conventional methods or random designs while achieving a similar mixing performance. Based on the NSGA-II designs, we have a better understanding about how to design a microfluidic mixer rationally: a mixer should have a constriction to increase contact area and contact time between the fluids, as well as some features that are not for mixing but rather for reducing the overall resistance of the mixer.

### 4.1 Limitations

The optimum mixer designs generated by our algorithm have certain constraints. Since the boundary conditions of our

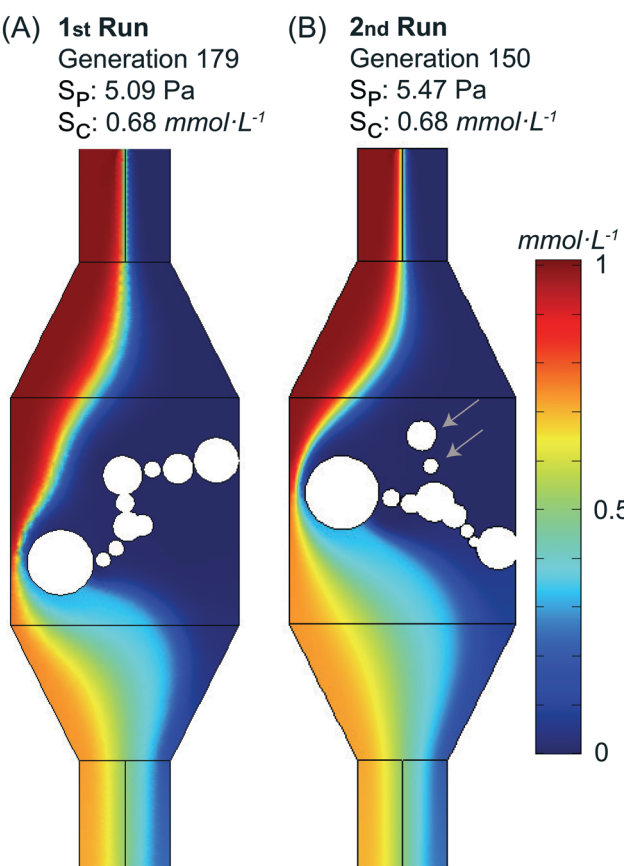


**Fig. 6** (A) The NSGA-II design selected at the end of the first run of evolution. (B) The NSGA-II design selected at the end of a second run of evolution. In the second run, the geometry converged into a Y-shape. To achieve a similar mixing score as the S-shaped design from run 1, the Y-shaped design from run 2 will have a higher fluidic resistance. Two gray arrows indicate the inefficient use of two posts by the NSGA-II algorithm, which seemed to only increase the resistance instead of improving the mixing performance.

optimizing system were set to a fixed value, the optimum mixer design is only investigated and experimentally verified when Reynold number is around 0.4. Our current work utilizes a constant volumetric flow rate to drive fluid flow. Since the two sets of inlet and outlet channels in our mixer chips have the same length and resistance to flow, we expect that our results would also hold true for pressure-driven flow using identical pressures at each inlet. It is possible that the optimal mixing features (the layout of posts) will change according to different boundary conditions. For instance, a certain optimum mixer design may still have potential to be optimized if we apply it on inertial microfluidics, centrifugal microfluidics or capillary microfluidics. As for other methods for driving fluid flow (like inertial, centrifugal, or capillary forces), as long as we can accurately model the physical phenomena involved in those methods, our micromixer generating algorithm can optimize those microfluidics designs based on the predicted results. Accurately modeling inertial, centrifugal, and capillary forces in microfluidics is itself a challenging and active research topic, one that is beyond the scope of this work. But as improved modeling techniques are developed in the future, these techniques can be integrated with our micromixer generating algorithm to develop optimal mixer designs for systems that utilize those forces.

In addition, our simulations were constrained in a 2-D plane, and the height of the channel was not defined. In theory, a 3-D simulation would be a more accurate way to capture the mixing and diffusion phenomenon. For instance, Stroock *et al.* designed a chaotic micromixer with a herringbone design in the bottom of the channels that could introduce mixing of different lamina in 3-D.<sup>22</sup> Cha *et al.* presented a PDMS-based micromixer with 3-D structures for rapid mixing performance.<sup>23</sup> However, the computational expense of implementing such a large number of simulations in 3-D was prohibitive for us. Therefore, the performance of 3-dimensional micromixers could not be compared with our optimum mixer designs.

#### 4.2 Future directions

Our approach is not limited to optimize only mixer performance—it should be able to optimize additional parameters as well. For instance, the overall chip size is also a key aspect of a microfluidic chip. Instead of constraining a mixer into a fixed design domain, we could try to minimize the size of the design domain as well. Additionally, microfluidic mixers are just one of many components in microfluidic chips.<sup>24,25</sup> We are confident that our approach can be applied to other applications of microfluidics. For example, cell sorting is a major application in microfluidics.<sup>26</sup> In various sorting technologies, inertial microfluidics shows the potential to efficiently separate different cells based on the sizes of cells.<sup>27–30</sup> However, inertial microfluidic devices are usually operated at a high Reynolds number, at which shear stress could be harmful to

the target cells.<sup>31</sup> In this case, coupled with our previous work (MOPSA, microfluidics-optimized particle simulation algorithm<sup>32</sup>), NSGA-II could be used to optimize an inertial microfluidic chip so as to increase the separation performance while minimizing the damage to cells from shear stress.

#### Conflicts of interest

There are no conflicts of interest to declare.

#### Acknowledgements

This work was supported by National Natural Science Foundation of China (No. 61827806 and 61871161).

#### References

- 1 C.-Y. Lee, C.-L. Chang, Y.-N. Wang and L.-M. Fu, *Int. J. Mol. Sci.*, 2011, **12**, 3263–3287.
- 2 C.-Y. Lee, W.-T. Wang, C.-C. Liu and L.-M. Fu, *Chem. Eng. J.*, 2016, **288**, 146–160.
- 3 C. Li and T. Chen, *Sens. Actuators, B*, 2005, **106**, 871–877.
- 4 D. E. Hertzog, B. Ivorra, B. Mohammadi, O. Bakajin and J. G. Santiago, *Anal. Chem.*, 2006, **78**, 4299–4306.
- 5 H. Wang, P. Iovenitti, E. Harvey and S. Masood, *J. Micromech. Microeng.*, 2003, **13**, 801.
- 6 H. Wang, P. Iovenitti, E. Harvey and S. Masood, *Smart Mater. Struct.*, 2002, **11**, 662.
- 7 S. Hossain, M. A. Ansari, A. Husain and K.-Y. Kim, *Chem. Eng. J.*, 2010, **158**, 305–314.
- 8 C. A. Cortes-Quiroz, A. Azarbadeegan, M. Zangeneh and A. Goto, *Chem. Eng. J.*, 2010, **160**, 852–864.
- 9 L.-M. Fu, W.-C. Fang, H.-H. Hou, Y.-N. Wang and T.-F. Hong, *Chem. Eng. J.*, 2014, **249**, 246–251.
- 10 L. Wang, S. Ma, X. Wang, H. Bi and X. Han, *Asia-Pac. J. Chem. Eng.*, 2014, **9**, 877–885.
- 11 J. Wang, P. Brisk and W. H. Grover, *Lab Chip*, 2016, **16**, 4212–4219.
- 12 K. Deb, A. Pratap, S. Agarwal and T. Meyarivan, *IEEE Trans. Evol. Comput.*, 2002, **6**, 182–197.
- 13 Z. Petrášek and P. Schwille, *Biophys. J.*, 2008, **94**, 1437–1448.
- 14 B. Ghasemishabankareh, M. Ozlen and X. Li, *International Conference on Evolutionary Multi-Criterion Optimization*, 2019, pp. 541–552.
- 15 M. Hesami, R. Naderi, M. Tohidfar and M. Yoosefzadeh-Najafabadi, *Front. Plant Sci.*, 2019, **10**, 869.
- 16 M. H. Shojaee-fard, S. E. Hosseini and J. Zare, *Struct. Multidiscip. Optim.*, 2019, 1–17.
- 17 S. Wang, D. Zhao, J. Yuan, H. Li and Y. Gao, *Electr. Power Syst. Res.*, 2019, **175**, 105893.
- 18 K. Deb, *Evol. Comput.*, 1999, **7**, 205–230.
- 19 E. Zitzler, K. Deb and L. Thiele, *Evol. Comput.*, 2000, **8**, 173–195.
- 20 Y. Xia and G. M. Whitesides, *Angew. Chem., Int. Ed.*, 1998, **37**, 550–575.

- 21 Autodesk, DXF Reference, 2011, [http://images.autodesk.com/adsk/files/autocad\\_2012\\_pdf\\_dxf-reference\\_enu.pdf](http://images.autodesk.com/adsk/files/autocad_2012_pdf_dxf-reference_enu.pdf).
- 22 A. D. Stroock, S. K. Dertinger, A. Ajdari, I. Mezić, H. A. Stone and G. M. Whitesides, *Science*, 2002, **295**, 647–651.
- 23 J. Cha, J. Kim, S.-K. Ryu, J. Park, Y. Jeong, S. Park, S. Park, H. C. Kim and K. Chun, *J. Micromech. Microeng.*, 2006, **16**, 1778.
- 24 G. M. Whitesides, *Nature*, 2006, **442**, 368.
- 25 T. M. Squires and S. R. Quake, *Rev. Mod. Phys.*, 2005, **77**, 977.
- 26 C. W. Shields IV, C. D. Reyes and G. P. López, *Lab Chip*, 2015, **15**, 1230–1249.
- 27 D. Di Carlo, *Lab Chip*, 2009, **9**, 3038–3046.
- 28 S. S. Kuntaegowdanahalli, A. A. S. Bhagat, G. Kumar and I. Papautsky, *Lab Chip*, 2009, **9**, 2973–2980.
- 29 S. C. Hur, N. K. Henderson-MacLennan, E. R. McCabe and D. Di Carlo, *Lab Chip*, 2011, **11**, 912–920.
- 30 A. A. S. Bhagat, H. W. Hou, L. D. Li, C. T. Lim and J. Han, *Lab Chip*, 2011, **11**, 1870–1878.
- 31 M. G. Lee, J. H. Shin, C. Y. Bae, S. Choi and J.-K. Park, *Anal. Chem.*, 2013, **85**, 6213–6218.
- 32 J. Wang, V. G. Rodgers, P. Brisk and W. H. Grover, *Biomicrofluidics*, 2017, **11**, 034121.